JACS
JOURNAL OF THE AMERICAN CHEMICAL SOCIETY

Article

pubs.acs.org/JACS

Understanding the Efficiency of Autonomous Nano- and Microscale Motors

Wei Wang,[†] Tso-Yi Chiang,[‡] Darrell Velegol,*[,‡] and Thomas E. Mallouk*[,†]

[†]Department of Chemistry and [‡]Department of Chemical Engineering, The Pennsylvania State University, University Park, Pennsylvania 16802, United States

Supporting Information

ABSTRACT: We analyze the power conversion efficiency of different classes of autonomous nano- and micromotors. For bimetallic catalytic motors that operate by a self-electrophoretic mechanism, there are four stages of energy loss, and together they result in a power conversion efficiency on the order of 10^{-9}. The results of finite element modeling agree well with experimental measurements of the efficiency of catalytic Pt−Au nanorod motors. Modifications of the composition and shape of bimetallic catalytic motors were predicted computationally and found experimentally to lead to higher efficiency. The efficiencies of bubble-propelled catalytic micromotors, magnetically driven flagellar motors, Janus micromotors driven by self-generated thermal gradients, and ultrasonically driven metallic micromotors are also analyzed and discussed.

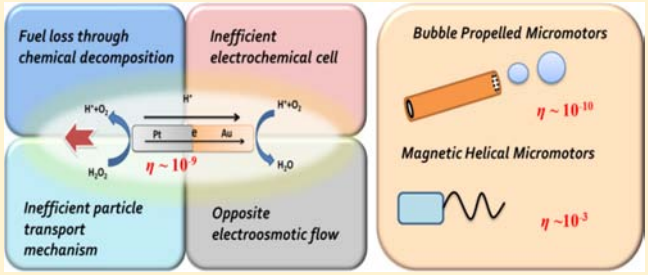

INTRODUCTION

Nano- and microscale motors are tiny objects that are capable of converting the energy of chemical fuels or external fields into mechanical motion.[1,2] Such motors are ubiquitous in the biological world, ranging from enzymatic assemblies that are nanometers in size to bacteria and cells in the range of micrometers to tens of micrometers. Synthetic motors that are similar in size to bacteria were first introduced in 2004−2005.[3,4] The first generation of these motors were 2−3 μm long bimetallic rods (Pt−Au and Ni−Au) that catalytically decomposed hydrogen peroxide to oxygen and water and moved at speeds in the range of 10 μm/s. Over the past decade, bimetallic catalytic motors have been redesigned for faster movement[5−9] and for functionality that includes sensing, pumping, and cargo delivery.[10−13] Microjets are a related class of tubular or conical catalytic motors that also catalyze hydrogen peroxide decomposition.[14−21] Unlike bimetallic nanorods, which are propelled by self-electrophoretic forces, microjets are propelled by bubble recoil and travel at impressively fast speeds, up to mm/s.[22] They have recently been studied for potential applications that include cell sorting and transport.[20,23−25] Magnetically driven motors are another emerging class of micromachines[26−31] which, like flagellar bacteria, convert the whiplike or rotary motion of their tails into axial translation.

While much effort has been devoted to increasing the speed and functionality of autonomous motors, few papers have commented on the efficiency with which they convert the free energy stored in fuel to mechanical energy. A power conversion efficiency on the order of 10^{-9} was estimated by Paxton et al. for Au−Pt nanorod catalytic motors in hydrogen peroxide solutions.[32] In contrast to these low experimentally measured efficiencies, the movement of nanodimers and catalytic nanoparticles has been studied in molecular dynamics simulations, and a maximum thermodynamic efficiency on the order of 10^{-4} was found for both systems.[33,34] However, the small size of these hypothetical nanomotors and their operation under idealized conditions (separate dimers with attractive or repulsive interdimer potentials and catalytic particles in gaseous fuels, respectively) makes it difficult to compare them with experimentally studied nano/micromotors. Sabass and Seifert found computationally that the efficiency of diffusiophoretic nano/micromotors should increase with decreasing motor size.[35,36] However, there are so far no studies that attempt to model and also measure the efficiencies of synthetic nano/micromotors (self-electrophoretic, bubble-propelled, magnetic, self-thermophoretic, and ultrasonically driven) that have been experimentally fabricated.

In contrast to synthetic motors, the efficiency of nano- and micromotors in biology is typically high. For example, kinesin-based microtubule motors have been estimated to have a chemical-to-mechanical power conversion efficiency of roughly 60%.[37,38] The efficiency of biological motors confers many advantages, including the ability to run for long periods of time using on-board fuel, and to use oxidants that are present in low concentration or consumed in slow catalytic reactions. For example, aerobic organisms are able to use oxygen in metabolic reactions despite its low concentration (~0.3 mM) in air-saturated water. Because synthetic nano/micromotors are many

Received: May 22, 2013
Published: June 24, 2013

   dx.doi.org/10.1021/ja405135f | J. Am. Chem. Soc. 2013, 135, 10557−10565

orders of magnitude less efficient, they are usually studied in solutions that contain high concentrations (~1 M) of hydrogen peroxide or other fuels. A broader choice of fuels (including, for example, glucose/oxygen) would be available to catalytic motors and pumps if their efficiency could be increased by 3−4 orders of magnitude or more. Understanding the sources of energy loss in these systems is thus important to broadening their range of useful properties and applications.

MATERIALS AND METHODS

Synthesis of Nanorods and Nanotubes. Bimetallic nanorods were fabricated as described in earlier publications.[39−42] Anodic alumina membranes (AAO, purchased from Whatman Inc., 200 nm nominal pore size) were used as templates for the electrodeposition of metals. The metal plating solutions were purchased from Technic, Inc. A 5 nm thick film of Cr and a 350 nm thick film of Ag were evaporated onto the branched pore side (hereafter called the back side) of the membranes by using a Kurt Lesker Lab-18 evaporator. This metal film served as the working electrode contact for electrodeposition. The lengths of the metal segments were controlled by monitoring the charge passed. The plating conditions for Ag, Au, and Pt were −1.77, −1.24, and −1.77 mA/cm^2, respectively. Ru was deposited at a constant potential of −0.65 V vs Ag/AgCl. Multisegment nanorods were synthesized by replacing the plating solution without disassembling the plating cell, with a water rinsing step in between. After the electrodeposition step, the membrane was thoroughly rinsed with deionized (DI) water and air-dried, and typically one-half of the membrane was soaked sequentially in 1:1 v/v HNO_3 and 0.5 M NaOH to dissolve the silver and the alumina template, respectively. The freed wires were then sonicated and washed in DI water several times until the pH was neutral. The yield of nanowires was roughly 2 × 10^9 per AAO membrane.

AuRu nanotubes were fabricated following the method of Shin et al.[43] A layer of gold was evaporated on the back side of a Whatman AAO 200 nm membrane. Then polyaniline was grown in the pores by sweeping the potential between −0.2 and 1.2 V vs Ag/AgCl for 50 cycles. The membrane was dried in a nitrogen stream and then soaked in 1 M NaOH for 4 min to slightly etch the side walls of the AAO pores. The membrane was thoroughly rinsed immediately after the NaOH etch and was then heated at 80 °C overnight. Together with the etching of the side wall, this heating step created a small gap between the polyaniline nanorods and the pore wall, thus enabling the deposition of metal nanotubes. The metals of interest were then sequentially deposited into the gap following ordinary electrodeposition procedures. Polyaniline was removed with concentrated HNO_3 after the deposition of the metal tubes.

Motor Tracking. The detailed procedure for tracking motor movement is described in earlier papers.[39] Bimetallic nanorods were suspended in aqueous 5% H_2O_2 solution for at least 15 min before they were taken for observation. An Olympus BX60M optical microscope (reflection mode) and a commercial video capturing bundle (Dazzle video creator plus) were used for observing the particles and recording videos, and typically an overall magnification of 500× or 1000× was used to take each video clip of 30 s at 30 frames/s. Dark field is ideal for observing the motion of nanorods due to the reflective nature of the metals. In most cases, the observation cell was a piece of rectangular glass capillary tubing (VitroTubeTM from VitroCom, 0.2 × 2.00 mm, catalog # 3520-050), which was filled with the nanorod suspension by capillarity.

The videos were then loaded into PhysMo 2, an open source tracking program (PhysMo - Video Motion Analysis Package, http://physmo.sf.net), and the coordinates of the metal rods were recorded as a function of time. Rod speed was calculated by dividing the displacement of the rod center between sequential frames by the time interval (0.033 s), and then taking the average of the speed over the selected tracking period. The tracking was repeated with multiple rods (at least 10 data points for each rod) to ensure statistically robust results.

In the experiments in which the wall effect was examined more closely, a different observation cell was used. In this case, a ring-shaped piece of double sided sticky tape was attached to a piece of glass slide (poly(ethyleneglycol) (PEG) coated or uncoated). A volume of 50 μL of nanorod suspension in 5% H_2O_2 solution was added to the center of the ring, and a glass coverslip was placed on top to seal the cell. The uncoated glass slide was precleaned in Piranha solution (concentrated H_2SO_4/30% H_2O_2 = 3:1. ***Caution!*** *Extremely corrosive! Protective equipment and care are needed when handling Piranha solutions!*). Au−Pt nanomotors moved at an average speed of 9 ± 2 and 14 ± 3 μm/s in cells made from uncoated glass slides and PEG-coated glass slides, respectively.

Oxygen Evolution Measurements. Nanorods of known concentration were mixed with aqueous 5% H_2O_2 for 15 min before each experiment. The suspension was transferred to a 10 mL test tube, which was sealed and purged with Ar before sampling. For each sample, 500 μL Ar was injected into the tube and a 500 μL gas sample was withdrawn and injected into a gas chromatograph. The oxygen evolution rate per wire was calculated after taking into account the oxygen from the air that had leaked in, the volume of gas in the head space and the number of wires in the suspension. A control experiment was carried out in the absence of catalytic nanorods with all the other experiential parameters the same. A typical result is shown in Figure S-1 (see Supporting Information).

RESULTS AND DISCUSSION

Self-Electrophoretic Catalytic Motors. While a number of mechanisms have been proposed to contribute to the propulsion of bimetallic motors in H_2O_2 solutions, there is good evidence that self-electrophoresis (Figure 1) is dominant

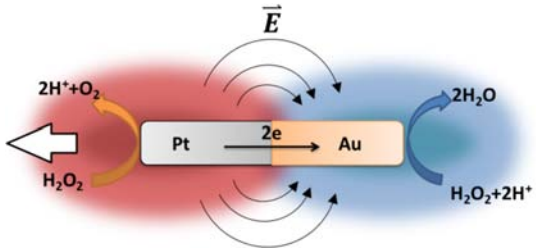

Figure 1. Illustration of the self-electrophoretic propulsion mechanism for a Au−Pt catalytic nanomotor. Red and blue represent high and low proton concentrations, respectively. The electric field **E**⃗ points from the anode (Pt) end to the cathode (Au). The white arrow indicates the direction of motion of the motor.

for motors in the size range of a few micrometers and below.[11,39] In this mechanism, the oxidation and reduction of H_2O_2 occur preferentially at the anode (Pt) and cathode (Au), respectively (eqs 1 and 2). This results in an asymmetric distribution of protons near the ends of the rod, which in turn creates an electric field in the solution near the metal rod. Because the metal surface is negatively charged, the rod moves in this self-generated electric field. It is worth noting that a significant portion of the cathodic current is contributed by the reduction of oxygen to water at the gold surface (eq 3).[39] However, this does not affect the propulsion mechanism or the product distribution in the overall reaction (eq 4).

$$\text{anode:}\quad H_2O_2(aq) \rightarrow 2H^+(aq) + O_2(g) + 2e^- \tag{1}$$

$$\text{cathode:}\quad H_2O_2(aq) + 2H^+(aq) + 2e^- \rightarrow 2H_2O(l) \tag{2}$$

$$\text{cathode:}\quad \frac{1}{2}O_2(g) + 2H^+(aq) + 2e^- \rightarrow H_2O(l) \tag{3}$$

dx.doi.org/10.1021/ja405135f | J. Am. Chem. Soc. 2013, 135, 10557−10565

$$\text{overall:}\quad 2H_2O_2(aq) \rightarrow 2H_2O(l) + O_2(g) \tag{4}$$

The power conversion efficiency of the nanomotor is defined by eq 5,

$$\eta_{overall} = \frac{\text{mechanical power output}}{\text{total chemical power input}} = \frac{P_{mecha}}{P_{chem}} \tag{5}$$

where P_{mecha} and P_{chem} are further defined as

$$P_{mecha} = F_{drag}v = fv^2 \tag{6a}$$

For spheres

$$f = 6\pi\mu r \tag{6b}$$

For cylinders

$$f = \frac{2\pi\mu L}{\ln\left(\frac{L}{R}\right) - 0.72} \tag{6c}$$

$$P_{chem} = n_{O_2}\Delta_r{}^{\theta}G \tag{7}$$

Here F_{drag} is the drag force on a spherical or cylindrical motor, μ is the dynamic viscosity of water, r is the radius of the spherical particle, L is the length of the cylindrical rod (3 μm), R is its radius (150 nm), v is the motor speed, n_{O_2} is the oxygen evolution rate in units of mol/(rod·s) and $\Delta_r{}^{\theta}G$ is the Gibbs free energy of the decomposition of H_2O_2 into water and oxygen (eq 4, −206 kJ per mole of O_2 produced). The mechanical work (= P_{mecha} × time) is the useful work done by the motors. From the O_2 evolution rate of Au−Pt nanorods in 5% H_2O_2 (Figure 2, left column), we obtained n_{O_2} = 2.3 × 10^{-15} mol O_2/(rod·s) and a H_2O_2 consumption rate of 2 × 2.3 × 10^{-15} = 4.6 × 10^{-15} mol/(rod·s). We note that this result is slightly higher than, yet on the same order as, the results from two previous experiments.[3,39]

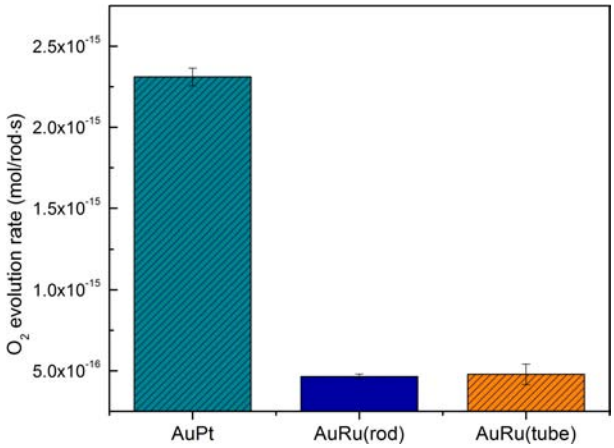

Figure 2. Gas chromatographic measurements of O_2 evolution rates from bimetallic motors: Au−Pt nanorods (left), Au−Ru nanorods (middle), and Au−Ru nanotubes (right). Error bars represent standard deviations from triplicate measurements.

From the oxygen evolution rate (Figure 2) and average axial velocity, the efficiency could be calculated from eqs 6b and 7. The speed of the Au−Pt nanomotors was 21 ± 4 μm/s, yielding an overall efficiency (sometimes referred to as a *thermodynamic efficiency*) of 7 × 10^{-9}, in rough agreement with previous report of Paxton et al.[32] The fastest moving self-electrophoretic nanomotors reported so far have a speed of ∼150 μm/s, with an Ag−Au alloy as the cathode.[6] If these motors consume fuel at the same rate as Au−Pt nanorods, their energy efficiency would be on the order of 10^{-7}.

There are four sources of loss that together result in the very low efficiency of bimetallic catalytic nanomotors. The first stage of energy loss comes from the chemical (or nonelectrochemical) decomposition of H_2O_2, which is catalyzed by Pt.[44] The fuel utilization efficiency can be expressed as

$$\eta_{fuel} = \frac{\text{electrochemical decomposition rate}}{\text{overall decomposition rate of fuel}} \tag{8}$$

The electrochemical decomposition rate was measured by Paxton et al. using Pt−Au interdigitated microelectrodes in H_2O_2 solutions of various concentrations, and a current density of 0.68 A/m^2 was found for 6% H_2O_2.[11] Although the geometry of that experiment was different from that of Au−Pt nanorods, the microelectrode current density provides a rough estimate of the electron transfer rate (and proton flux) at the nanomotor surface. Using this value, we obtain 7 × 10^{-6} mol/(m^2·s) for these fluxes, and the electrochemical H_2O_2 decomposition rate can be calculated as 0.5−1.1 × 10^{-17} mol/(rod·s), depending on the balance of reactions 2 and 3 at the cathode. From the total decomposition rate of H_2O_2 (4.6 × 10^{-15} mol/(rod·s)), we then obtain η_{fuel} = 1.1 × 10^{-3} to 2.3 × 10^{-3}. Because Wang et al. found that eq 3 is the dominant cathode reaction,[2] we estimate η_{fuel} to be approximately 1 × 10^{-3} for Au−Pt nanorod motors.

It is apparent from this calculation that the efficiency of nanorod motors could be increased by a factor of ∼10^3 by using metals that selectively catalyze H_2O_2 oxidation and reduction without catalyzing the overall decomposition reaction. Substitution of Ru for Pt lowers the rate of O_2 evolution by 80% (Figure 2) and Au−Ru nanorods move at similar speed (18 ± 3 μm/s) to Au−Pt (21 ± 4 μm/s), resulting in a 4-fold increase in efficiency. However, Ru is still very catalytically active and decomposes roughly 99% of the fuel chemically, rather than electrochemically. A recent report by Liu and Sen describes self-electrophoretic Cu−Pt nanomotors that operate in dilute Br_2 or I_2 solutions.[45] Since the spontaneous reaction of Br_2 or I_2 at the Cu surface of the Cu−Pt nanomotors is not significant, these nanomotors are ∼10^3 times more efficient than Pt−Ru nanorods in H_2O_2 solutions and are thus able to move at speeds up to 20 μm/s in solutions of ∼2 mM halogen.

A second stage of energy loss arises from the use of a very exoergic reaction to generate a small potential drop along the surface of the nanomotor. The electrochemical potential of the cell (eq 4) can be calculated as 1.07 V from eq 9:

$$\Delta_r{}^{\theta}G = -nFE_{cell} \tag{9}$$

In contrast, the potential difference ($\Delta\phi$) in the solution between the two ends of a Au−Pt nanomotor, at a surface proton flux of 7 × 10^{-6} mol/(m^2·s), was found by finite element simulations (see the Supporting Information) to be only 2.1 mV. A cell efficiency term is defined by eq 10 to represent this stage of energy loss:

$$\eta_{cell} = \frac{\Delta\phi}{E_{cell}} = \frac{2.1\text{ mV}}{1.07\text{ V}} \tag{10}$$

For the Au−Pt catalytic nanomotors, η_{cell} is ∼2 × 10^{-3}. It is interesting to contrast this value with the near-unit efficiency of biological motors that are driven by proton gradients, such as ATP synthetase. The biological motors operate near the

dx.doi.org/10.1021/ja405135f | J. Am. Chem. Soc. 2013, 135, 10557−10565

reversible limit through a tight coupling of mechanical work to the movement of protons down (or up) a pH gradient. In the present case, the proton gradient and resulting electric field established by the reaction are depolarized by convection, by electromigration, and especially by rapid diffusion of protons from the anode to the cathode, as we show below.

Referring to Figure 1, oxidation and reduction occur preferentially at the Pt and Au ends of the nanorods, respectively. Protons are generated at the Pt end and consumed at the Au end, leading to a concentration gradient of protons around the rod (see Figure S5a for the numerically simulated proton concentration profile). The concentration gradient drives protons by diffusion from the anode to the cathode. In addition, protons are subject to migration in the same direction in the self-generated electric field, and also move by convection in the frame of the moving rod. The counterion HCO_3^- is subject to the same effects (the solution is exposed to the air and CO_2 is dissolved in the solution; see eq S4 in the Supporting Information), but its migration is in the opposite direction. The transport of ions is governed by the general flux equation (eq 11),

$$J_i = uc_i - D_i\nabla c_i - \frac{z_i D_i F c_i \nabla\phi}{RT} \quad (11)$$

where J_i is the flux of ion i and the three terms on the right represent convection, diffusion, and elecromigration, respectively. Far from the surface of the motor, the flux and each of the gradient terms are zero, but at the motor surface J_{H+} is related to the current density j by $J_{H+} = j/F$. Here u is the fluid velocity, ϕ is the electrostatic potential, F is the Faraday constant, R is the gas constant, T is the absolute temperature, and c_i, D_i, and z_i are the concentration, diffusion coefficient and charge of species i, respectively.

The respective contributions of diffusion, electromigration and convection to the transport of protons can be estimated by numerical simulation (Figure 3; see the Supporting Information for details). For protons moving along the long axis of the nanorod, electromigration is dominant, contributing ~68% of the overall flux. The diffusive flux is ~29%, and convection is relatively unimportant at ~3% (Figure 3b). On the other hand, for proton transport away from and toward the nanorod (perpendicular to the direction of motion), diffusion accounts for nearly 99% of the overall flux (Figure 3c), while proton transport by electromigration and convection are negligible.

This simulation shows that the diffusion and electromigration fluxes, which are both proportional to D_{H+}, the diffusion coefficient of protons (eq 11), are together responsible for the dissipation of the proton gradient generated by the electrochemical reaction at the Pt–Au nanorod surface. Thus, the value of D_{H+}, which is 9.3×10^{-5} cm^2/s in pure water at 25 °C,[46] can affect the speed and efficiency of the motor. By varying the diffusion coefficient of protons in the numerical model, the calculated motor speed could be varied by a factor of 3, as shown in Figure 4. Moran et al. found that the speed of self-electrophoretically driven motors is inversely proportional to the proton diffusion coefficient in their scaling analysis of the Au–Pt nanomotor system.[47] Although the result obtained by numerical modeling in Figure 4 is not strictly inversely proportional, it shows a similar trend. We note that the purpose of this simulation is to demonstrate how diffusion coefficient affects the motor behavior; experimentally, the diffusion coefficient of any ion in water cannot surpass that of protons.

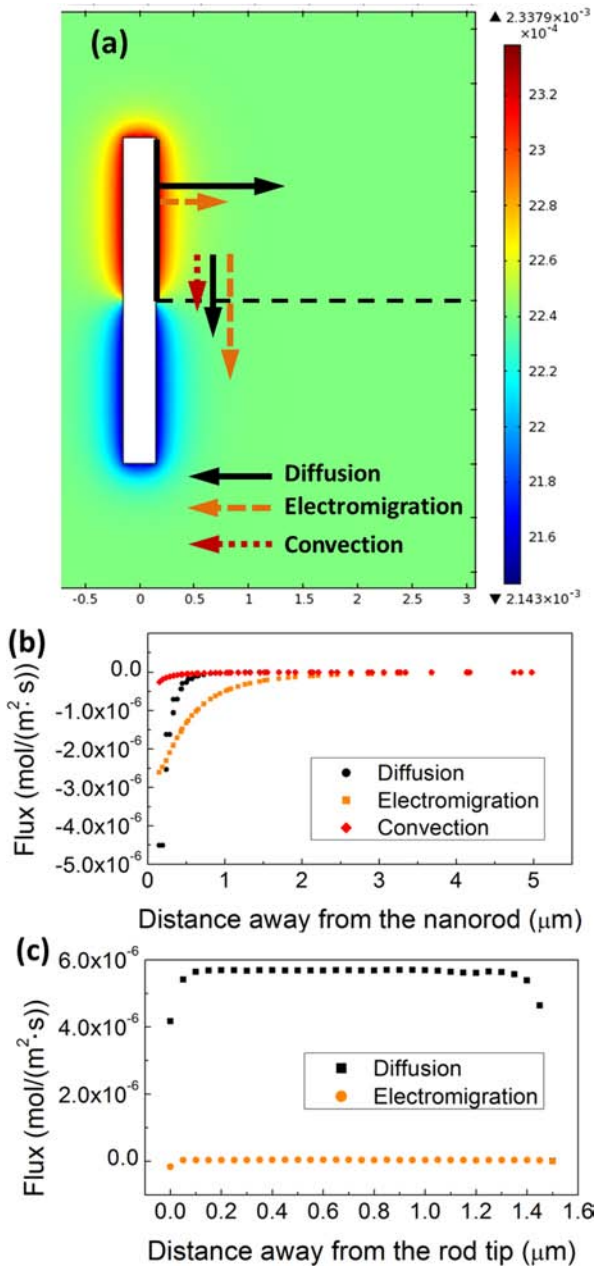

Figure 3. Numerical simulation to determine the contributions of diffusion, electromigration, and convection to proton transport. (a) Steady-state proton distribution around a Pt (top)-Au (bottom) catalytic nanomotor (3 μm long and 300 nm in diameter) with a surface flux of 7×10^{-6} mol/(m^2·s). Red and blue represent high and low proton concentrations (units in legend: mol/m^3). Arrows illustrate proton flux contributions (arrow lengths are not in exact proportion to the flux). The units for the x axis are μm. (b) Proton fluxes from diffusion, electromigration, and convection along the nanorod long axis across the center line (dashed line in (a)). (c) Proton fluxes perpendicular to the nanorod surface from the top half (Pt end, across the black line in (a)). In (b) and (c), fluxes were integrated over the respective cross sections.

Experimentally, it is difficult to manipulate the proton diffusion coefficient without significantly altering other parameters of the system, such as viscosity or temperature. However, it is possible to limit proton diffusion by spatial confinement. In order to test this hypothesis, we fabricated bimetallic nanotubes in which both the inner and outer surfaces

dx.doi.org/10.1021/ja405135f | J. Am. Chem. Soc. 2013, 135, 10557–10565

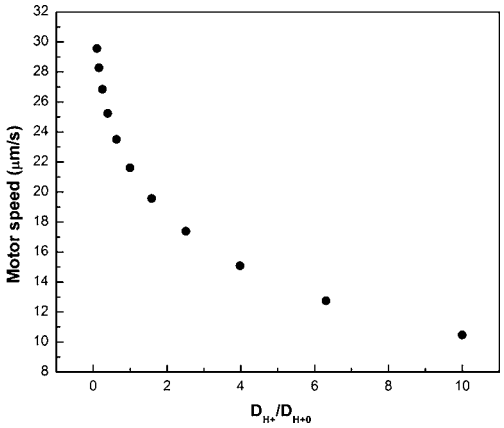

Figure 4. Relationship between the proton diffusion coefficient (D_{H+}) and the motor speed from numerical simulations. D_{H+0} is the experimental proton diffusion coefficient in water. In the model, the D_{H+}/D_{H+0} ratio was arbitrarily varied between 0.1 to 10.

were catalytically active. These tubular nanomotors, as a result, were predicted to generate a higher proton flux and also inhibit diffusion of protons out of the tube, thus significantly increasing the electric field and consequently the motor speed.

Numerical modeling of these tubular nanomotors shows that they indeed trap protons inside the tube and increase the local proton concentration significantly (see Figures S11 and S12). We fabricated Au−Ru nanotubes by a modification of the template-assisted electrodeposition process described by Shin et al.[43] Figure 5 shows field emission SEM images and a cartoon of the structure of these nanotubes.

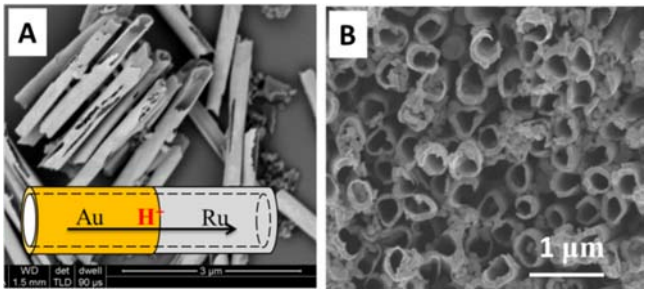

Figure 5. FESEM images of Au−Ru nanotubes: (a) side and (b) end-on view.

The Au−Ru nanotubes moved at a speed of 32 ± 5 μm/s in 5% H_2O_2 solution, roughly 75% faster than solid Au−Ru nanorods of similar dimensions (18 ± 3 μm/s). The nanotubes moved with their Au end leading, and no bubbles were observed, consistent with the self-electrophoretic mechanism. Gas chromatographic measurements showed that the rates of O_2 evolution from nanotubes and nanorods were the same within experimental error. Because the drag force scales as v^2 (eq 6), the efficiency of the tubular Au−Ru motor is higher than that of cylindrical Au−Ru and Au−Pt motors by factors of 3 and 12, respectively.

The fact that oxygen was not produced at a significantly faster rate from the Au−Ru nanotubes than from Au−Ru nanorods suggests that mass transfer of H_2O_2 into the tubes is limited by their geometry. As a result, the decomposition of H_2O_2 on the inner surface is slower and produces a lower flux of protons than on the outside of the tube. Nevertheless, simulations show that even if the flux on the inner surface is only 10% of that on the outer surface, a significantly higher proton concentration develops inside the tube (see Figure S12).

The third stage of energy loss concerns the fraction of electrical energy, represented as the potential difference between the anode and cathode ($\Delta\phi$), that is converted into mechanical work. The nanomotor equivalent circuit can be represented as a DC voltage source in series with the solution resistance, as illustrated in Figure 6.

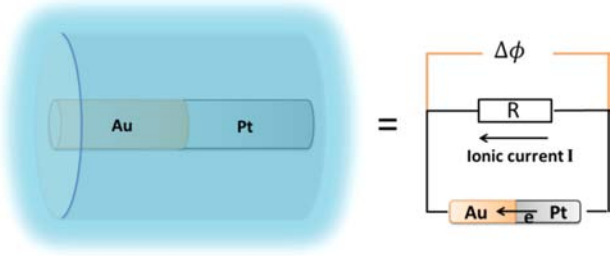

Figure 6. Equivalent circuit of the nanomotor-solution system. The blue cylinder around the bimetallic nanorod represents the solution near its surface, which is represented as a resistor in the equivalent circuit on the right.

For this stage we can define the propulsion efficiency by eq 12:

$$\eta_{prop} = \frac{P_{mecha}}{P_{elec}} = \frac{P_{mecha}}{\Delta\phi I} \tag{12}$$

where P_{mecha} is the mechanical power of the nanomotor (3.3×10^{-18} W/rod from eq 6), P_{elec} is the electrical power that is generated by the calculated 2.1 mV potential difference ($\Delta\phi$), and I is the current flowing in the system. Taking the current density to be 0.68 A/m^2 and the surface area of each segment of the rod as 1.48×10^{-12} m^2, the current is 1.0 pA. Therefore, P_{elec} is 2.1×10^{-15} W/rod and η_{prop} is 1.6×10^{-3}, or on the order of 10^{-3}. This component of the overall motor efficiency is sometimes referred to as the *hydrodynamic efficiency*.

The inherently low efficiency of this stage can be understood in terms of the electrophoretic force acting on a charged particle. This is most simply modeled for a Janus sphere of radius r, for which the electrophoretic velocity v is

$$v \sim \frac{\zeta\varepsilon_r\varepsilon_0 E}{\mu} \sim \frac{\zeta\varepsilon_r\varepsilon_0\Delta\phi}{\pi r\mu} \tag{13}$$

Here, ζ is the zeta potential of the particles, which Paxton et al. measured as −40 mV for Au rods in deionized water.[11] The electric field E can be approximated as the potential drop ($\Delta\phi$) divided by the path length l around the sphere, πr. The other terms in the equation are ε_r, the relative permittivity of water (80.1), ε_0 the vacuum permittivity (8.854×10^{-12} F/m), and μ, the viscosity of water (1×10^{-3} N·s/m at 293 K). The drag force and the mechanical power of the Janus sphere are given by eq 6.

The electrical power can be calculated as the current−voltage product, that is,

$$P_{elec} = jA\Delta\phi = 2\pi r^2 j\Delta\phi \tag{14}$$

dx.doi.org/10.1021/ja405135f | J. Am. Chem. Soc. 2013, 135, 10557−10565

where j is the current density and A is the area of one-half of the Janus sphere, which equals $2\pi r^2$. Combining eqs 13 and 14, we obtain the efficiency as

$$\eta_{\text{prop}} = \frac{P_{\text{mecha}}}{P_{\text{elec}}} = \frac{6\pi\mu r v^2}{2\pi r^2 j\Delta\phi} \approx \frac{3(\zeta\varepsilon_r\varepsilon_0)^2\Delta\phi}{\pi^2 r^3 \mu j} \quad (15)$$

The last term in this equation can be simplified by expressing $\Delta\phi/j$ in terms of the resistivity ρ of the solution, which Paxton et al. measured as 2.5×10^3 Ω·m for suspensions of gold nanorods in water.[11] Making the simplifying assumption that the area (A') through which ion current flows in the solution is equal to the area (A) of the hemisphere (i.e., that electrons and ions have the same current densities in the system), we have

$$\frac{\Delta\phi}{j} = \frac{A\Delta\phi}{I} = AR \approx A\left(\frac{\rho l}{A'}\right) \approx \pi r\rho \quad (16)$$

Combining these equations, we obtain

$$\eta_{\text{prop}} \approx \frac{3(\zeta\varepsilon_r\varepsilon_0)^2\rho}{\pi r^2\mu} \quad (17)$$

Substituting the values given above with $r = 1$ μm, we calculate $\eta_{\text{prop}} \approx 2 \times 10^{-3}$, in reasonable agreement with the measured value. This result shows that electrophoretic energy transduction should be inherently inefficient with motors in the micrometer (and larger) size regimes, especially in electrolyte solutions with low ρ (e.g., high ionic strength). The $1/r^2$ scaling of η_{prop} suggests that submicrometer swimmers might have higher efficiency. However, A/A' will also decrease as r decreases, to some extent canceling this effect.

The fourth stage of energy loss for bimetallic catalytic motors is the electroosmotic flow of fluid at the bottom of the glass cell, which opposes the direction of electrophoretic propulsion for negatively charged nanorods. Because the nanorods are made of dense metals, they sink to an equilibrium position slightly above the bottom wall of the cell. Their height above this glass surface is determined by a balance of the downward gravitational force and the electrostatic repulsion between the rod and the glass. The electroosmotic counter-flow is illustrated in Figure 7.

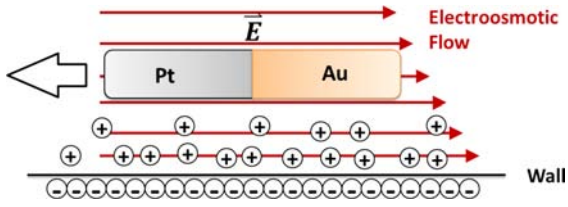

Figure 7. A self-electrophoretic nanomotor generates an electric field, which induces electroosmotic flow along the charged wall of the cell in the opposite direction.

Because of the close proximity of the nanomotor to the wall (500 nm to 1 μm), the effect of electroosmotic flow can be significant. In fact, there are cases where local electroosmotic flow dominates over the electrophoretic transport of particles and causes them to move in the opposite direction.[11,48,49] To further confirm the existence of the reverse electroosmotic flow and to estimate its effect on the motors, we compared the movement of Au−Pt nanomotors suspended in 5% H_2O_2 over an uncoated glass slide and one coated with poly(ethyleneglycol) (PEG). The PEG coating imparts a smaller (∼ −10 mV) charge to the surface.[50−52] Nanomotors moved ∼60% faster over this surface than they did over uncoated glass slides, which typically have zeta potentials of −60 to −90 mV.[53] Taking into account that the mechanical power of the nanomotor scales as the square of its velocity (eq 6), we can define an efficiency related to this wall effect:

$$\eta_{\text{wall}} = \left(\frac{v}{v_0}\right)^2 \quad (18)$$

where v is the observed velocity of nanomotors with the wall effect and v_0 is the velocity of motors in its absence of the effect. Based on the difference in the speeds for nanomotors moving near walls of different zeta potentials, we can estimate $\eta_{\text{wall}} \leq 0.4$.

This effect can be minimized by lowering the charge density of the wall, as illustrated in the PEG experiment. However, the nanorods are maintained above the wall by electrostatic propulsion, and they adhere to walls of opposite charge. Thus, a more thorough analysis is needed to evaluate the optimal surface charge on the bottom wall that gives the highest efficiency. An alternative is to increase the negative surface charge on the nanomotor, which should increase its speed and, through electrostatic repulsion, its distance from the bottom wall.

The energy loss due to the wall effect is approximately a factor of 2, which is less significant than the other three energy loss pathways, each of which have values of about 10^{-3}. The wall effect can however be important for large and/or dense micromotors. In such cases, the distance between the motor and the wall is small compared to the size of the motor. In the presence of a large cargo particle, depending on its dimensions and density, the wall effect could generate stronger backward electroosmotic flow or hydrodynamic drag that significantly slows down the motor.

Catalytic Bubble Motors. It is interesting to compare the efficiency of self-electrophoretic motors with those that utilize other propulsion mechanisms. In two cases, the propulsion efficiencies are relatively straightforward to estimate: micromotors driven by bubble propulsion[14,17,18,54] and magnetically driven helical micromotors.[26,28,29] These two types of motors have been well studied and are being investigated for a variety of applications, including those in biological environments.[20,22,24,25,55]

Tubular catalytic micromotors, first reported by Solovev et al.,[14] are propelled by oxygen bubbles generated by the catalytic decomposition of H_2O_2. Motors of different dimensions and with different bubble production rates result in different velocities. For example, multilayered 5.5 μm diameter microtubes 100 μm in length were reported to move through 3% H_2O_2 solution at 50 μm/s.[14] In 3% H_2O_2, the microtubes generate 34 μm radius bubbles at a rate of 1.5 per second. Using the ideal gas law, the oxygen evolution rate is 1.10×10^{-11} mol/(tube·s), corresponding to a chemical input power of 2.27×10^{-6} W/tube. The mechanical power output can be calculated from the velocity (eq 6c), to be 5.46×10^{-16} W/tube. The ratio gives an efficiency of 2.40×10^{-10}, which is comparable to that of self-electrophoretic nanomotors. A similar analysis applied to bubble-powered Janus sphere micromotors[56] gives a calculated efficiency of 5×10^{-10}.

The low efficiency of bubble-powered micromotors can be understood in terms of two stages of energy loss. The expansion of the oxygen gas into bubbles large enough to detach from the particle surface is a prerequisite to motion. The

dx.doi.org/10.1021/ja405135f | J. Am. Chem. Soc. 2013, 135, 10557−10565

expansion power of the oxygen bubbles can be estimated, assuming the ideal gas law and reversible expansion, to be 2.50 × 10^{-8} W/jet. Thus, the work of bubble expansion constitutes ∼1% of the chemical input energy, and 99% of the energy of the reaction is dissipated as heat at this stage. The second stage of energy loss derives from the fact that, at low Reynolds number, propulsion happens only at the instant of bubble release. Careful examination of microtube motion has shown that the motors are stationary except for sharp spikes of movement corresponding to bubble release.[19] At low Reynolds number (10^{-4}–10^{-5}), the time scale of acceleration and deceleration is on the order of microseconds, and the recoil movement persists only over this short time period. Further, because the momentum of the bubble and motor must be equal and opposite at the instant of release, some of the kinetic energy goes into the bubble and the viscous layer of water between its surface and the shear plane. The combination of these effects apparently results in a second-stage efficiency of ∼10^{-8} for bubble motors, making their overall efficiency ∼10^{-10}.

Magnetic Micromotors. It is also interesting to consider the efficiency of magnetic micromotors, which incorporate flexible chains made of superparamagnetic colloidal particles,[31] partially dissolved nanowires,[30] or helix shaped microparticles.[26,28] This class of micromotors is especially interesting because of their resemblance to flagella bacteria, which combine the helical form of the synthetic motors with catalytic propulsion. In an externally applied rotating magnetic field, helical magnetic motors rotate. The torque applied to the helical tail translates into an axial force, which results in directional motion of the micromotors. The torque, axial force, linear velocity, and angular velocity of the motor can be related via a 2 × 2 Purcell matrix[57]

$$\begin{bmatrix} F \\ N \end{bmatrix} = \begin{bmatrix} a & b \\ b & c \end{bmatrix} \begin{bmatrix} v \\ \Omega \end{bmatrix} \tag{19}$$

where F is the axial force (which equals the drag force on the micromotor at low Reynolds number), N is the torque (in N·m) due to the applied magnetic field, v is the axial speed of the motor, and Ω is the angular speed (in rad/s). This matrix gives the efficiency, η:

$$\eta = \frac{\text{mechanical power output}}{\text{power input}} = \frac{Fv}{N\Omega} \tag{20}$$

This calculation does not take into account the magnetic energy absorbed by the medium surrounding the motor, or the heat generated in the electrical circuit that controls the magnet. It accounts only for the mechanical energy imparted by magnetic induction and the fraction of that energy that is converted to axial movement. Thus, η represents an upper limit for the efficiency of the motor.

Among several reports on helical magnetic micromotors, one by Nelson et al. provides details about the Purcell matrix, axial force, and torque.[26] For a 38 μm micromotor in a 2 mT magnetic field, the Purcell matrix was found to be

$$\begin{bmatrix} a & b \\ b & c \end{bmatrix} = \begin{bmatrix} 1.5 \times 10^{-7} & -1.6 \times 10^{-14} \\ -1.6 \times 10^{-14} & 2.3 \times 10^{-19} \end{bmatrix} \tag{21}$$

As a result the maximum drag force, torque, angular velocity, and motor velocity were derived as 3.0 × 10^{-12} N, 4.3 × 10^{-17} N·m, 190 rad/s, and 1.8 × 10^{-5} m/s, respectively. These values give η = 0.66%, that is, on the order of 10^{-2}–10^{-3}. This is slightly higher than the hydrodynamic propulsion efficiency of electrophoretically (10^{-3}) or diffusiophoretically driven (10^{-3})[35,36] motors in the micrometer size range.

The hydrodynamic efficiency of these helical motors is comparable to that of flagellar bacteria. Purcell calculated that the maximum efficiency of rotating flagella is ∼1%.[58] The experimental efficiency of *E. coli* propulsion has been estimated to be around 2%.[59,60] Purcell has pointed out that the energy consumption of a flagellar bacterium is negligible compared to its energy intake in an environment in which nutrition is abundant. Propulsion mechanisms of modest efficiency are therefore biologically viable in such cases.

Other Micromotors. We briefly analyze the power conversion efficiency of two other micromotor systems. Self-thermophoretic motors are Janus microspheres half-coated with gold[61,62] or Permalloy.[63] They move autonomously in liquids due to a photothermally or magnetically induced asymmetric temperature gradient in the fluid surrounding the sphere. Jiang et al. found that 1 μm diameter silica microspheres half-coated with a 25 nm gold layer were propelled in water at 6 μm/s,[58] yielding a mechanical power output of 3 × 10^{-19} W (eq 6a). The energy input was 1046 nm light, with 40 mW focused into a 9 μm diameter beam. Assuming an absorbance of ∼1%[64] for the gold cap, the power input was ∼5 × 10^{-6} W, yielding an energy efficiency on the order of 10^{-13}–10^{-14}.

Recently, Wang et al. have shown that metallic microrods undergo autonomous motion in ultrasonic standing waves at MHz frequency.[65] These microrods move at axial speeds up to ∼200 μm/s. The propulsion force is thought to arise from a small pressure difference induced by scattering of acoustic energy at the concave and convex ends of the asymmetric microrods. In these experiments, a piezoelectric transducer operating at 250 mW was coupled to a 25 cm^2 stainless steel plate. Because the microrods (3 μm long and 300 nm in diameter) are much smaller than the wavelength (∼400 μm), the effective cross-sectional area for acoustic scattering can be roughly approximated as area as a circle whose diameter is the length of the rods (3 μm). Assuming that the acoustic power is distributed uniformly across the area of the cell, the power input to a single motor is ∼7 × 10^{-10} W. The mechanical power of the micromotors is estimated from the speed and drag force to be 2 × 10^{-16} W (eq 6c). This gives an energy efficiency on the order of 10^{-7}.

■ CONCLUSIONS

Both self-electrophoretic and bubble-powered catalytic micromotors have efficiencies, defined as the fraction of chemical input energy that is converted to mechanical work, on the order of 10^{-9}–10^{-10}. These low efficiencies can be understood in semiquantitative terms as sequential stages of energy loss. A broader range of functionality could be available to catalytic micromotors if their efficiency could be increased by 3–4 orders of magnitude, including operation using dissolved O_2 as the oxidant. The simplest path to increasing the efficiency of self-electrophoretic motors is to eliminate the background catalytic consumption of fuel, and this idea has already been demonstrated with bimetallic copper-halogen micromotors.[45]

The low efficiency with which chemically generated potential gradients are converted to mechanical work (the third stage of energy loss, eq 17) suggests that self-electrophoretic micromotors have an upper limit of efficiency of 10^{-3}–10^{-4}. Natural catalytic motors circumvent this problem by directly coupling

the power stroke of chemical bond making or breaking to mechanical movement. It is interesting that both helical magnetic micromotors and acoustic motors are orders of magnitude more efficient than self-electrophoretic motors. They may have a broader range of potential applications, especially if some of the interesting functionality of catalytic motors (such as chemotaxis and other collective phenomena) can be realized with these propulsion mechanisms.

■ ASSOCIATED CONTENT

Supporting Information

A typical oxygen evolution measurement result, SEM images of the nanorods, numerical modeling details and results, and description of the calculation of motor speed based on fluid speed. This material is available free of charge via the Internet at http://pubs.acs.org.

■ AUTHOR INFORMATION

Corresponding Author

velegol@psu.edu; tem5@psu.edu

Notes

The authors declare no competing financial interest.

■ ACKNOWLEDGMENTS

We thank Ayusman Sen, Vin Crespi, Amir Nourhani, and Shoji Hall for helpful discussions, Shahrzad Yazdi, Anand Kumar Singh, and Abdul Aziz for help with modeling software, Wentao Duan for the help with zeta potential measurements, and San-Hoon Yoo for the help with the synthesis of nanotubes. Work at Penn State was supported by the National Science Foundation under MRSEC Grant DMR-0802404 and IDR CBET 1014673. Analytical instrumentation used in this work was supported by the Pennsylvania State University Materials Research Institute Nanofabrication Laboratory under National Science Foundation Cooperative Agreement No. ECS-0335765.

■ REFERENCES

(1) Mallouk, T. E.; Sen, A. *Sci. Am.* **2009**, 72.
(2) Ozin, G. A.; Manners, I.; Fournier-Bidoz, S.; Arsenault, A. *Adv. Mater.* **2005**, *17*, 3011.
(3) Paxton, W. F.; Kistler, K. C.; Olmeda, C. C.; Sen, A.; St Angelo, S. K.; Cao, Y.; Mallouk, T. E.; Lammert, P. E.; Crespi, V. H. *J. Am. Chem. Soc.* **2004**, *126*, 13424.
(4) Fournier-Bidoz, S.; Arsenault, A. C.; Manners, I.; Ozin, G. A. *Chem. Commun.* **2005**, 441.
(5) Sattayasamitsathit, S.; Gao, W.; Calvo-Marzal, P.; Manesh, K. M.; Wang, J. *ChemPhysChem* **2010**, *11*, 2802.
(6) Demirok, U. K.; Laocharoensuk, R.; Manesh, K. M.; Wang, J. *Angew. Chem., Int. Ed.* **2008**, *47*, 9349.
(7) Laocharoensuk, R.; Burdick, J.; Wang, J. *ACS Nano* **2008**, *2*, 1069.
(8) Zacharia, N. S.; Sadeq, Z. S.; Ozin, G. A. *Chem. Commun.* **2009**, 5856.
(9) Balasubramanian, S.; Kagan, D.; Manesh, K. M.; Calvo-Marzal, P.; Flechsig, G. U.; Wang, J. *Small* **2009**, *5*, 1569.
(10) Campuzano, S.; Kagan, D.; Orozco, J.; Wang, J. *Analyst* **2011**, *136*, 4621.
(11) Paxton, W. F.; Baker, P. T.; Kline, T. R.; Wang, Y.; Mallouk, T. E.; Sen, A. *J. Am. Chem. Soc.* **2006**, *128*, 14881.
(12) Wu, J.; Balasubramanian, S.; Kagan, D.; Manesh, K. M.; Campuzano, S.; Wang, J. *Nat Commun* **2010**, *1*, 36.
(13) Jun, I. K.; Hess, H. *Adv. Mater.* **2010**, *22*, 4823.
(14) Solovev, A. A.; Mei, Y.; Bermúdez Ureña, E.; Huang, G.; Schmidt, O. G. *Small* **2009**, *5*, 1688.
(15) Mei, Y.; Solovev, A. A.; Sanchez, S.; Schmidt, O. G. *Chem Soc Rev* **2011**, *40*, 2109.
(16) Huang, G. S.; Wang, J. S.; Mei, Y. F. *J. Mater. Chem.* **2012**, *22*, 6519.
(17) Gao, W.; Sattayasamitsathit, S.; Orozco, J.; Wang, J. *J. Am. Chem. Soc.* **2011**, *133*, 11862.
(18) Manesh, K. M.; Cardona, M.; Yuan, R.; Clark, M.; Kagan, D.; Balasubramanian, S.; Wang, J. *ACS Nano* **2010**, *4*, 1799.
(19) Li, J. X.; Huang, G. S.; Ye, M. M.; Li, M. L.; Liu, R.; Mei, Y. F. *Nanoscale* **2011**, *3*, 5083.
(20) Solovev, A. A.; Sanchez, S.; Pumera, M.; Mei, Y. F.; Schmidt, O. G. *Adv. Funct. Mater.* **2010**, *20*, 2430.
(21) Sanchez, S.; Solovev, A. A.; Mei, Y. F.; Schmidt, O. G. *J. Am. Chem. Soc.* **2010**, *132*, 13144.
(22) Sanchez, S.; Ananth, A. N.; Fomin, V. M.; Viehrig, M.; Schmidt, O. G. *J. Am. Chem. Soc.* **2011**, *133*, 14860.
(23) Solovev, A. A.; Xi, W.; Gracias, D. H.; Harazim, S. M.; Deneke, C.; Sanchez, S.; Schmidt, O. G. *ACS Nano* **2012**, *6*, 1751.
(24) Balasubramanian, S.; Kagan, D.; Jack Hu, C.-M.; Campuzano, S.; Lobo-Castañon, M. J.; Lim, N.; Kang, D. Y.; Zimmerman, M.; Zhang, L.; Wang, J. *Angew. Chem., Int. Ed.* **2011**, *50*, 4161.
(25) Campuzano, S.; Orozco, J.; Kagan, D.; Guix, M.; Gao, W.; Sattayasamitsathit, S.; Claussen, J. C.; Merkoçi, A.; Wang, J. *Nano Lett.* **2011**, *12*, 396.
(26) Zhang, L.; Abbott, J. J.; Dong, L.; Peyer, K. E.; Kratochvil, B. E.; Zhang, H.; Bergeles, C.; Nelson, B. J. *Nano Lett.* **2009**, *9*, 3663.
(27) Zhang, L.; Petit, T.; Lu, Y.; Kratochvil, B. E.; Peyer, K. E.; Pei, R.; Lou, J.; Nelson, B. J. *ACS Nano* **2010**, *4*, 6228.
(28) Ghosh, A.; Fischer, P. *Nano Lett.* **2009**, *9*, 2243.
(29) Tottori, S.; Zhang, L.; Qiu, F.; Krawczyk, K. K.; Franco-Obregon, A.; Nelson, B. J. *Adv. Mater.* **2012**, *24*, 811.
(30) Gao, W.; Sattayasamitsathit, S.; Manesh, K. M.; Weihs, D.; Wang, J. *J. Am. Chem. Soc.* **2010**, *132*, 14403.
(31) Dreyfus, R.; Baudry, J.; Roper, M. L.; Fermigier, M.; Stone, H. A.; Bibette, J. *Nature* **2005**, *437*, 862.
(32) Paxton, W. F.; Sen, A.; Mallouk, T. E. *Chem.—Eur. J.* **2005**, *11*, 6462.
(33) Shi, Y.; Huang, L.; Brenner, D. W. *J. Chem. Phys.* **2009**, *131*, 014705.
(34) Tao, Y. G.; Kapral, R. *J. Chem. Phys.* **2009**, 131.
(35) Sabass, B.; Seifert, U. *J. Chem. Phys.* **2012**, 136.
(36) Sabass, B.; Seifert, U. *Phys. Rev. Lett.* **2010**, 105.
(37) Iwatani, S.; Iwane, A. H.; Higuchi, H.; Ishii, Y.; Yanagida, T. *Biochemistry* **1999**, *38*, 10318.
(38) Block, S. M. *Cell* **1998**, *93*, 5.
(39) Wang, Y.; Hernandez, R. M.; Bartlett, D. J.; Bingham, J. M.; Kline, T. R.; Sen, A.; Mallouk, T. E. *Langmuir* **2006**, *22*, 10451.
(40) Hernández, R. M.; Richter, L.; Semancik, S.; Stranick, S.; Mallouk, T. E. *Chem. Mater.* **2004**, *16*, 3431.
(41) Kline, T. R.; Tian, M.; Wang, J.; Sen, A.; Chan, M. W. H.; Mallouk, T. E. *Inorg. Chem.* **2006**, *45*, 7555.
(42) Mbindyo, J. K. N.; Mallouk, T. E.; Mattzela, J. B.; Kratochvilova, I.; Razavi, B.; Jackson, T. N.; Mayer, T. S. *J. Am. Chem. Soc.* **2002**, *124*, 4020.
(43) Shin, T.-Y.; Yoo, S.-H.; Park, S. *Chem. Mater.* **2008**, *20*, 5682.
(44) McKee, D. W. *J. Catal.* **1969**, *14*, 355.
(45) Liu, R.; Sen, A. *J. Am. Chem. Soc.* **2011**, *133*, 20064.
(46) *CRC Handbook of Chemistry and Physics*, 93rd ed.; Taylor & Francis, Inc., CRC Press: Boca Raton, FL, 2012.
(47) Moran, J.; Wheat, P.; Posner, J. *Phys. Rev. E* **2010**, *81*, 065302.
(48) Kline, T. R.; Paxton, W. F.; Wang, Y.; Velegol, D.; Mallouk, T. E.; Sen, A. *J. Am. Chem. Soc.* **2005**, *127*, 17150.
(49) Ibele, M. E.; Wang, Y.; Kline, T. R.; Mallouk, T. E.; Sen, A. *J. Am. Chem. Soc.* **2007**, *129*, 7762.
(50) Grabinski, C.; Schaeublin, N.; Wijaya, A.; D'Couto, H.; Baxamusa, S. H.; Hamad-Schifferli, K.; Hussain, S. M. *ACS Nano* **2011**, *5*, 2870.
(51) Wattendorf, U.; Merkle, H. P. *J. Pharm. Sci.* **2008**, *97*, 4655.

(52) Otsuka, H.; Nagasaki, Y.; Kataoka, K. *Adv. Drug Delivery Rev.* **2012**, *64*, 246.
(53) Sze, A.; Erickson, D.; Ren, L. Q.; Li, D. Q. *J. Colloid Interface Sci.* **2003**, *261*, 402.
(54) Gao, W.; Uygun, A.; Wang, J. *J. Am. Chem. Soc.* **2012**, *134*, 897.
(55) Solovev, A. A.; Sanchez, S.; Mei, Y. F.; Schmidt, O. G. *Phys. Chem. Chem. Phys.* **2011**, *13*, 10131.
(56) Gibbs, J. G.; Zhao, Y. P. *Appl. Phys. Lett.* **2009**, *94*, 163104.
(57) Purcell, E. M. *Am. J. Phys* **1977**, *45*, 3.
(58) Purcell, E. M. *Proc. Natl. Acad. Sci. U.S.A.* **1997**, *94*, 11307.
(59) Li, G.; Tang, J. X. *Biophys. J.* **2006**, *91*, 2726.
(60) Chattopadhyay, S.; Moldovan, R.; Yeung, C.; Wu, X. L. *Proc. Natl. Acad. Sci. U.S.A.* **2006**, *103*, 13712.
(61) Jiang, H. R.; Yoshinaga, N.; Sano, M. *Phys. Rev. Lett.* **2010**, 105.
(62) Qian, B.; Montiel, D.; Bregulla, A.; Cichos, F.; Yang, H. *Chem. Sci.* **2013**, *4*, 1420.
(63) Baraban, L.; Streubel, R.; Makarov, D.; Han, L.; Karnaushenko, D.; Schmidt, O. G.; Cuniberti, G. *ACS Nano* **2012**, *7*, 1360.
(64) Barnes, P. Y.; Early, E. A.; Parr, A. C. *NIST Measrurement Services: Spectral Reflectance*; U.S. Government Printing Office: Washington, D.C., 1998.
(65) Wang, W.; Castro, L. A.; Hoyos, M.; Mallouk, T. E. *ACS Nano* **2012**, *6*, 6122.